scientific reports

Check for updates

OPEN

Polarization dependent bound states in continuum in a tetramer metasurface discovered by random forest algorithm

Chenjie Jia[1], Zhenyu Zhao[1]✉ & Jun Wang[2]

A tetramer metasurface with strong coupling of meta-atoms under C_2 symmetry is proposed to realize polarization-dependent bound states in continuum (BICs) with the random forest regressor algorithm assistance. The quality (Q) factor of quasi-BIC correlates with the centralization degree of the tetramer structure, which is determined by the photonic band characteristics. The quasi-BIC is dominated by a hybrid of electric dipole and quadrupole in E_x polarization ($Q > 10^4$), whereas only electric dipole dominates quasi-BIC ($Q > 10^3$) in E_y polarization. These findings demonstrate a novel strategy to achieve ultrahigh Q-factor resonances in terahertz photonics.

Keywords Tetramer metasurface, Bound states in continuum, Terahertz wave, Machine learning

Metasurfaces composed of artificial electromagnetic subwavelength structures operating at THz frequencies (1 THz = 10^{12} Hz) are emerging as potential ultrasensitive biosensors[1–5]. This is due to their ability to confine incident electromagnetic energy locally and enhance light-matter interactions. Such local energy enhancement leads to ultrahigh Q-factors in the THz band, which increases the detection sensitivity of biological analytes, such as insulin[1]microorganisms[2] streptavidin–agarose[3] and antibiotics[4]. Therefore, achieving ultrahigh Q-factor resonances is crucial for realizing label-free, non-invasive THz biosensors[6,7] images[8] and holography[9] etc.

Bound states in the continuum (BICs) are highly localized states within the continuous spectrum of propagating modes in the surrounding space. These states do not interact with other states in the continuum and possess infinite Q-factors due to their infinite lifetimes, protected by symmetry[7,10–18]. The simplest systems for achieving BICs involve those where the coupling of certain resonances to radiation modes is forbidden due to symmetry or separability.

The tetramer metasurface exhibits inherent symmetry and offers large tunability of coupling parameters, positioning it as a new star in BICs research[19–23]. Previous studies focus on tetramers with all meta-atoms in C_4 symmetry. However, due to electromagnetic wave duality, breaking the C_4 symmetry is a necessity to achieve quasi-BICs (Q-BIC). In systems with C_2 symmetry, the wave-vector is non-conserved, resulting in $T_{xx} \neq T_{yy}$ for transmitted radiation electric components along the x and y axes[24].

If a tetramer structure with C_4 symmetry incorporates meta-atoms with C_2 symmetry, it is possible to achieve BICs without breaking the intrinsic symmetry of the tetramer or meta-atoms. To verify our hypothesis, we propose a metasurface with tetramer structures and calculate its THz response as a function of degree of centralization. Each unit cell comprises four identical meta-atoms in C_2 symmetry. The meta-atom is constructed using dual gap split-ring resonators (DSRR), featuring two gaps located in the middle of the top and bottom arms, respectively. The four meta-atoms are positioned concentrically within the tetramer's geometric center. Machine Learning (ML) or Artificial Neuro Network (ANN) is becoming novel tools to boost the design of metamaterials and metasurfaces[25–27] in which the Random Forest (RF) regressor algorithm can leverage a relatively tiny dataset to analyze the frequency response and Q-factors as functions of structure modification with proper accuracy and avoid overfitting[28–32]. Further discussions on the BIC generation mechanisms involve calculations of photonic band structures, electromagnetic field distributions, and multipolar decompositions.

[1]Department of Physics, Shanghai Normal University, 100 Guilin Road, Shanghai 200234, China. [2]Shaanxi Key Laboratory of Artificially Structured Functional Materials and Devices, Air Force Engineering University, Xi'an 710051, Shaanxi, China. ✉email: zyzhao@shnu.edu.cn

Results

This work identifies a polarization-dependent Q-BIC determined by the degree of centralization of a tetramer structure metasurface with C_2 symmetry. By leveraging the Random Forest algorithm, we reveal the THz transmittance spectra as functions of structural parameters and frequency. Both *x*-and-*y* polarized THz radiation can excite BIC at 1.25 THz and both *Q*-factors of corresponding Q-BICs exhibit an inverse-square relationship with the degree of centralization. Notably, the *Q*-factor of Q-BIC excited by *x*-polarized THz wave ($Q > 10^4$) is larger than that excited by *y*-polarized THz wave ($Q > 10^3$) at the same degree of centralization. The photonic band structure of the tetramer metasurface reveals a band gap along the Γ-M and Γ-X directions, which depends on the polarization of incident THz waves due to C_2 symmetry. Furthermore, the electromagnetic field distribution and multipolar decomposition reveal the ratio of dipoles, quadrupoles, and toroidal dipole modes contributing to Q-BIC behavior. Our results demonstrate a new type of metasurface exhibiting Q-BIC behavior with the assistance of Random Forest algorithm, and we realize the strong-coupling mechanism excited by incident THz waves under *x*-and-*y* polarization. This offers a new route for achieving ultra-high *Q*-factor THz metasurfaces for biosensor applications.

Metasurface structure

The geometry of the tetramer structures is illustrated in Fig. 1(a). Each meta-atom comprises a square-shaped metallic disc scatterer DSRR with lateral arms of length $l = 60$ μm and a gap size $g = 3$ μm, located at the midpoint between the top and bottom arms. The displacement distance between the meta-atom center and its boundary is $d = 37.5$ μm. A tetramer unit cell consists of four DSRRs arranged in a 2×2 configuration, with a lattice period $p = 150$ μm. As shown in Fig. 1(a), each meta-atom is displaced toward the geometry center of the tetramer. The degree of centralization α can be defined as follows:

$$\alpha = (\Delta d / d) \times 100\% \tag{1}$$

where Δd varies within the range of $-6.5\ \mu m \le \Delta d \le 6.5\ \mu m$ in the *xy*-plane at a spatial step of 0.25 μm when simulating with the software. The metallic layer of the DSRR is a 0.1 μm thick gold (Au) layer, deposited on a 75 μm-thick polyimide substrate. The tetramer metasurface is in *xy*-plane, and the wave-vector of incident THz wave is along the *z*-axis. The schematic diagram is illustrated in Fig. 1(b). The THz wave incidence is considered in two polarization modes: *x*-polarization E_x, where the electric component is perpendicular to the DSRRs' gaps and *y*-polarization E_y, where the electric component is parallel to the DSRRs' gaps. The periodic boundary condition as well as other parameters for simulation in described in the section of methods.

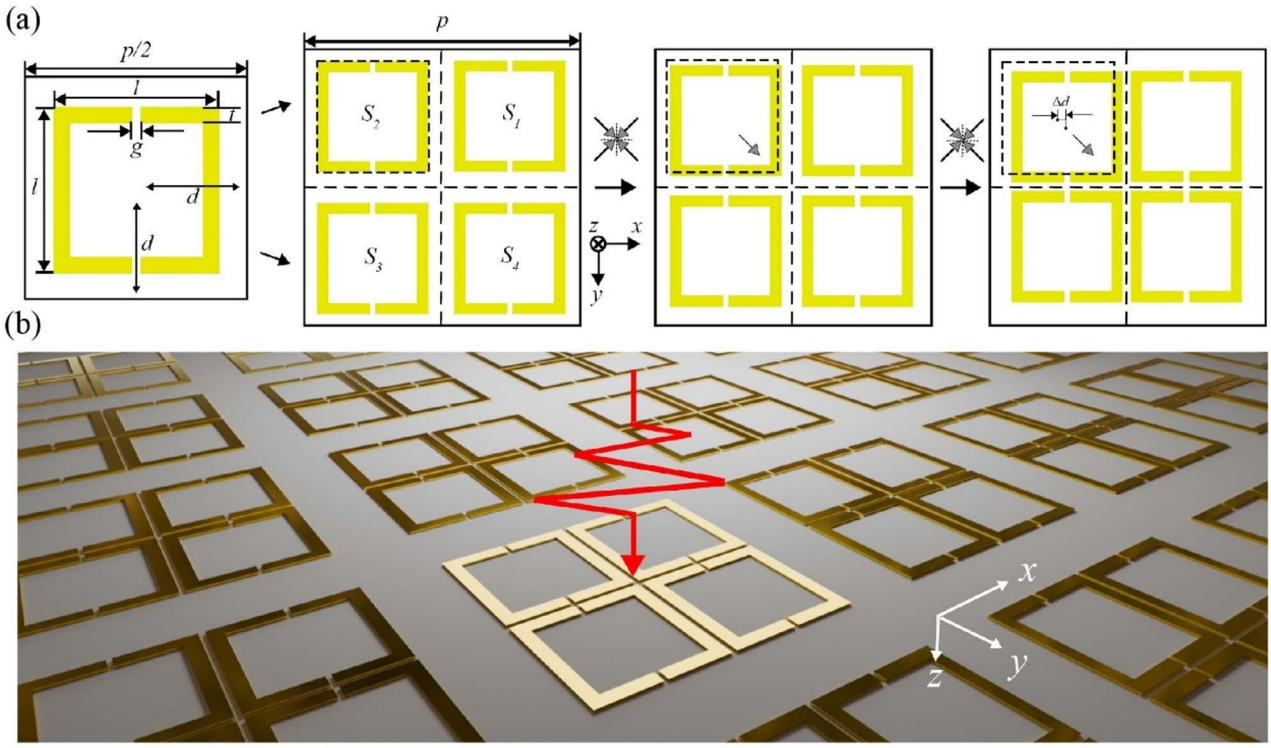


Fig. 1. Structure and excitation setup. (**a**) The C_2 centrosymmetric tetrameter unit cell, composed of four DSRRs. (**b**) A schematic illustrating a terahertz pulse (red line) incident normally on the lattice groups.

Simulation based results, RF prediction and evaluation

Full results under both procedures

Figure 2(a) and (b) show the simulated THz transmittance of tetramer meta-atoms at four displacements ($\Delta d = 0$ μm, $\Delta d = 2.1$ μm, $\Delta d = 4.3$ μm, $\Delta d = 6.5$ μm). The datasets align well with the predictions from the RF algorithm across both E_x and E_y polarization. Figure 2(c) and (d) provide detailed maps of THz transmittance as functions of frequency and displacement. These images clearly reveal BICs at 1.25 THz because no radiation is coupled to the incident THz wave.

As displacement increases ($\Delta d > 0$ μm), the tetramer exhibits centralization behavior, leading to energy leakage in the THz spectrum. This phenomenon indicates mode coupling with incident waves of x and y polarization, resulting in quasi-BICs that exhibit Fano-resonance line shapes. These can be fitted using the formula provided[12,33]:

$$T = \left| a_1 + ja_2 + \frac{b}{(\omega - \omega_0 + j\gamma)} \right|^2 \tag{2}$$

where a_1, a_2, and b are real numbers, ω_0 and γ are the center frequency and damping rate of the Fano-resonance. Q-BIC exhibits a redshift when the tetramer is excited by an E_x-polarized wave, while it undergoes a blueshift when excited by an E_y-polarized wave. The degree of centralization increases from 0 to 17.3%, causing quasi-BIC to shift from 1.250 THz to 1.245 THz under E_x excitation, whereas it shifts up to 1.27 THz under E_y excitation.

According to the definition of Q factor of quasi-BIC, the Q factor as a function of displacement can be calculated as below[12]:

$$Q = \omega_0 / 2\gamma \tag{3}$$

Figures 2(e) and (f) manifest the predicted Q factors of tetramer metasurfaces at different degrees of centralization. These results demonstrate an inverse-square relationship with the degree of centralization[12]:

$$Q \propto \alpha^{-2} \tag{4}$$

The observed behavior corresponds to the symmetry-protected BIC (SP-BIC), which relies on the degree of asymmetry. At the same level of centralization, the Q-factors of the Q-BICs depend on the polarization of incident terahertz waves. As shown in Fig. 2(e) and (f), the E_x-polarization incidence mode can achieve a higher

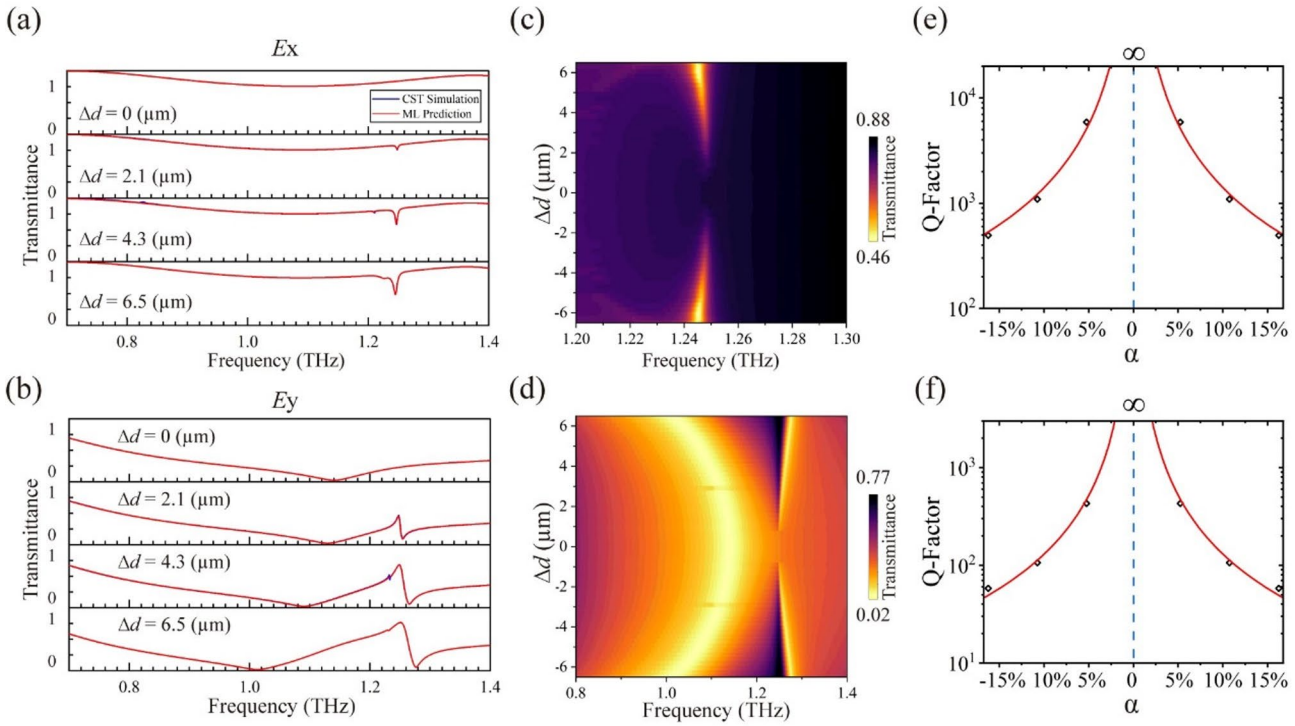


Fig. 2. (**a**) Transmittance as a function of frequency of tetramer metasurface under E_x-excitation. (**b**) Transmittance as a function of frequency of tetramer metasurface under E_y-excitation. Purple solid-line: CST simulation results. Red solid-line: RF prediction. (**c**) 2D map of THz transmittances as a function of frequency and displacement Δd of tetramer metasurface under E_x-excitation and (**d**) for E_y-excitation. (**e**) Q factors derived from the ML predictions under E_x-excitation and (**f**) for E_y-excitation. The red solid-line: inverse square dependence of displacement Δd.

Type	Q-factor
Biosensor[12]	$>10^3$
Biosensor[7]	$>10^2$
Asymmetric SRR[14]	$>10^1$
This work	$>10^4$

Table 1. The *Q*-factors comparison of different quasi-BICs.

Method	Δd = 0	Δd = 2.1	Δd = 4.3	Δd = 6.5
Euclidean distance	0.02998	0.004380	0.10038	0.36317
MAE	0.00091	< 0.00001	0.00212	0.00676

Table 2. Similarity evaluation.

Q-factor ($Q>10^4$) than the E_y-polarization incidence mode ($Q>10^3$). This difference arises from the photonic band structure and electromagnetic field distribution, as explained in the following section.

Table 1 shows a comparison between *Q*-factors under different designations. Our tetramer metasurface outperform well to these cutting-edged and traditional researches, which manifested an enormous potential to the applicational field.

RF prediction and evaluation

Data-driven RF algorithm is employed to identify potential Q-BIC patterns in the sparse input dataset derived from a 50 × 1001 simulation under CST Microwave Studio™. The prediction dataset matrix is expanded from its original size to 1000 × 2000. Performance evaluation metrics are calculated under the Euclidean distance formula[34]:

$$dis = \sqrt{\sum_{i=1}^{n} (x_i - \hat{x}_i)^2} \tag{5}$$

and Mean Absolute Error (MAE)[34]:

$$MAE = \frac{1}{n} \sum_{i=1}^{n} |x_i - \hat{x}_i| \tag{6}$$

where x_i is the actual (simulated) value, $\hat{x}_i$ is the predicted value and n represents sample data.

Table 2 presents the evaluation metrics for model performance. The results indicate that the RF regressor successfully achieves pattern recognition and generates accurate transmittance data. Compared to an artificial neuronal network (ANN)-based deep learning method, the RF algorithm demonstrates superior performance in terms of computational efficiency and model simplicity. This approach can reduce further simulation time from a few days down to a few seconds.

Band structure

Figure 3 presents the photonic band structure in the first Brillouin zone of the tetramer metasurface when $\Delta d = 0$ μm, alongside the *Q* factor as a function of the wavevector *k*. In Fig. 3(a), the band gap is observed to be nearly closed along the Γ-M direction but opens along the Γ-X direction, where the BIC band resides within the continuum band. The emergence of BICs occurs at this stationary state, as indicated by the red solid lines highlighting specific bands in Fig. 3(b). The BIC-associated band is located at the Γ point ($k=0$). The *Q* factors exhibit an infinite value at this point, corresponding to a sharp resonance and decrease steadily as the wavevector moves away from this point along the Γ-M direction. However, the *Q* factor abruptly drops along the Γ-X direction, representing the discrete spectrum in band structure cannot support the quasi-BIC.

In Fig. 3(c), an asymmetry in the band structure is observed, with the band gap opening differently along the Γ-M and Γ-X directions compared to previous. For the Γ-X direction, the BIC band approaches the forbidden band, and its *Q* factors again achieve an infinite value at the Γ point, corresponding to a sharp resonance. *Q* factors decrease steady as the wavevector moves away from this point along the Γ-X direction, whereas drops abruptly along the Γ-M direction. The differentia further confirming the distinct characteristics of the two types of BICs within the tetramer metasurface structure.

Electric fields and corresponding multipolar decomposition analysis

Upon absorption of light in material, electrons and/or holes with excess energy (hot carriers) can be created. The excess energy depends on a photon energy as well as a material band structure. In metals, photon absorption can take place through both interband and intraband within the conduction band-transitions, which is facilitated

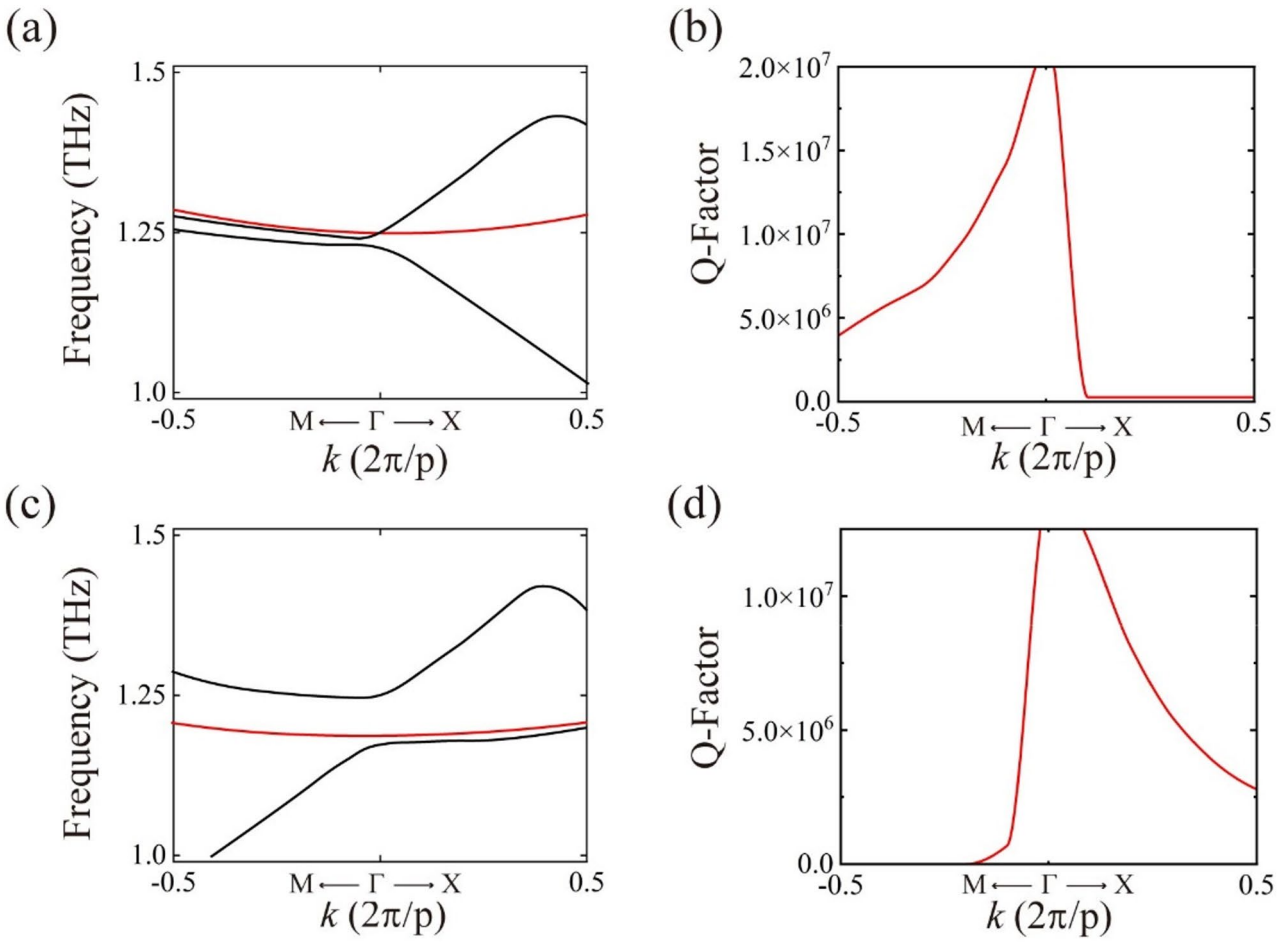


Fig. 3. The band structures of lattices and their corresponding quality factors. (**a**) The band structure for *x*-polarization mode. (**b**) The quality factors of the labeled band in (**a**) along the M-Γ-X direction. (**c**) The band structure for *y*-polarization mode. (**d**) The quality factors of the labeled band in (**c**) along the M-Γ-X direction.

by plasmonic excitations[35]. However, the intrinsic surface plasmon frequency of metal are much higher than the THz band[22]. Alternatively, the spoof surface plasmon rather than surface plasmon dominate the optical response of metallic metasurface at THz band[36]. Figure 4(a) and (c) shows the electric field distributions at the most centralized state when $\Delta d = 6.5$ μm. Under the E_x-excitation mode, Fig. 4(a) is dominated by electric dipole modes with strong positive and negative field regions forming along the *x*-axis, and added with quadrupole at midcourt line creates a superimposed pattern. Figure 5(a) sketched the overlay pattern. Dipole patterns are evident with the directional surface current arrows. The close spacing between metasurface DSRRs enhances coupling and create a continuous and symmetric dipole field distribution. Decreased interval leads the dipole fields to twist the quadrupole at midcourt line. These localized patterns indicate massive interaction between adjacent DSRRs. The dominance of dipole modes in E_x aligns with the *x*-polarized incident field, which excites these lower-order resonances effectively.

E_y electric field distributions in Fig. 4(c) demonstrate dual dipole-dominated responses. The coupling in the tetramer leads to a symmetric field distribution that orthogonal to the E_x-mode. The surface current arrows indicate alternating field directions along *y*-axis. One weak dipole locates in the middle of the tetramer and another stronger but inverse dipole surround at the top-arm of upside two DSRRs and bottom-arm of downside two DSRRs. Figure 5(b) sketched the dual dipoles schema. These results demonstrate the tetramer metasurface's capability to support and control superimposed ED-MD mode or overlay dual ED modes. Coupling strength or incident discrepancy can offer precise tuning of field localization, distribution and polarizations' domination. This makes the metasurface ideal for versatile usage from ultrasensitive biosensor to other complex circumstances.

Multipolar decomposition is leveraged to precisely quantify the contributions of each multipole: Electric Dipole (ED), Magnetic Dipole (MD), Electric Quadrupole (EQ), Magnetic Quadrupole (MQ) and Toroidal Dipole (TD), comparing to the observed resonances. This allows to calculate the scattering powers of each individual multipole within a Cartesian coordinate system, providing a detailed breakdown of the underlying mechanisms responsible for the resonance behavior.

Each defined as:

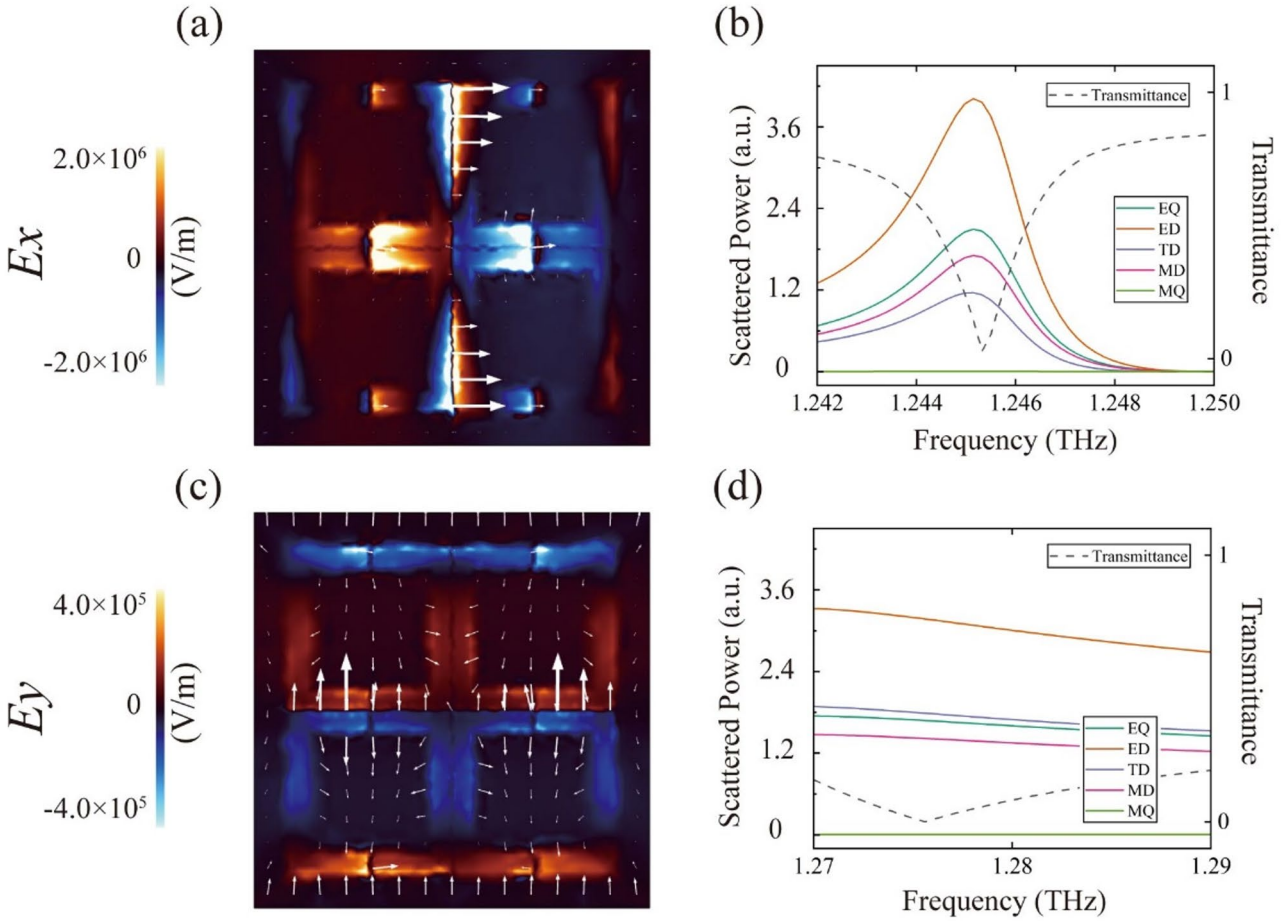


Fig. 4. Electric distributions and scattering powers of different multipoles in the transmission spectra of the meta-atoms, excited by E_x and E_y terahertz waves, when $\Delta d = 6.5$. (**a**) The electric field distributions under E_x. (**b**) Corresponding multipolar decomposition (**c**) The electric field distributions under E_y. (**d**) Corresponding multipolar decomposition. White arrow: Surface current. Color bar: Intensity. Orange: Electric Dipole (ED), Magenta: Magnetic Dipole (MD), Blue: Electric Quadrupole (EQ), Green: Magnetic Quadrupole (MQ), Purple: Toroidal Dipole (TD).

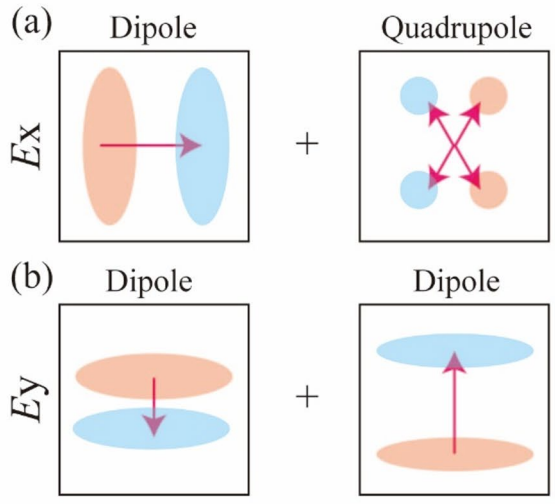


Fig. 5. Schematic diagram of multipoles contributing to the quasi-BIC excited by the terahertz waves in (**a**) E_x and (**b**) E_y polarization at $\Delta d = 6.5$ μm.

$$\overrightarrow{ED} = \frac{1}{iw}\int \vec{j}\, d^3r \tag{7}$$

$$\overrightarrow{MD} = \frac{1}{2C}\int (\vec{r} \times \vec{j}) d^3r \tag{8}$$

$$\overrightarrow{TD} = \frac{1}{10c}\int \left[\left(\vec{r}\cdot\vec{j}\right)\vec{r} - 2r^2\vec{j}\right] d^3r \tag{9}$$

$$EQ = \frac{1}{2i\omega}\int \left[r_\alpha j_\beta + r_\beta j_\alpha - \frac{2}{3}\left(\vec{r}\cdot\vec{j}\right)\delta_{\alpha,\beta}\right] d^3r \tag{10}$$

$$MQ = \frac{1}{3c}\int \left[\left(\vec{r}\times\vec{j}\right)_\alpha r_\beta + \left(\vec{r}\times\vec{j}\right)_\beta r_\alpha\right] d^3r \tag{11}$$

And then, far-field scattered power of them can be expressed in terms of the following formulas:

$$I_{ED} = \frac{2\omega^4}{3c^3}\left|\overrightarrow{ED}\right|^2 \tag{12}$$

$$I_{MD} = \frac{2\omega^4}{3c^3}\left|\overrightarrow{MD}\right|^2 \tag{13}$$

$$I_{TD} = \frac{2\omega^4}{3c^3}\left|\overrightarrow{TD}\right|^2 \tag{14}$$

$$I_{EQ} = \frac{\omega^6}{5c^5}\sum |EQ_{\alpha\beta}|^2 \tag{15}$$

$$I_{MQ} = \frac{\omega^6}{5c^5}\sum |MQ_{\alpha\beta}|^2 \tag{16}$$

where c and ω are the speed and angular frequency for light, respectively. $\alpha, \beta = x, y, z$ axis and $j = -i\omega\varepsilon_0(n^2-1)E^2$ is the current density distribution in meta-atoms[7,37,38].

Figure 4(b) and (d) illustrate the structural scattering power and transmittance of the metasurface, revealing a correlation between coupling states and resonance in Q-BIC. For E_x-polarization mode in Fig. 4(a), ED dominates Q-BIC, followed by EQ, MD, and TD. MQ has a negligible effect, with a magnitude several orders of magnitude lower than the others. The scattering power peaks at resonance frequency and rapidly decreases as it moves away from resonance. For E_y-polarization mode in Fig. 4(d), at the strongest coupling state, ED's contribution is significantly larger than TD, EQ, and MD. MQ can be excluded. The scattering spectra and transmittance indicate enhanced coupling between multipolar modes. Notably, the scattering power remains flat at the Q-BIC frequency in Fig. 4(b). As shown in Fig. 2(e) and (f), this characteristic leads to a lower Q-factor of Q-BIC excited under E_y-polarized radiation compared to E_x-polarized radiation at the same degree of centralization,

Methods

Simulation settings

The initial data for THz transmittance as a function of frequency are simulated using numerical platform CST Microwave Studio™. Periodic boundary conditions are applied in the *xy*-plane, while perfectly matched layers (PMLs) are implemented along the *z*-direction to prevent reflections. The polyimide substrate has a permittivity of 3.5 and a loss tangent of 2.7×10^{-3}. The conductivity of the lossy gold (Au) layer is 4.561×10^7 s/m. The initial simulations utilize the frequency-domain (FD) solver of CST Microwave Studio™ with a tetrahedral polygonal mesh for accurate calculations. To construct a dense mesh for better simulation results, the cell per max model box edge of the maximum cell is set to 25 in our model and 8 for the background. The mesh contains 124,526 tetrahedrons and slightly varied according to the specific lattice pattern (Δd difference). Additionally, COMSOL Multiphysics™ is employed to calculate the photonic band structure, electromagnetic field distribution, and multipoles decomposition.

Random forest pattern recognition

As a well-established machine learning method, Random Forest (RF) algorithm combines multiple decision trees to enhance predictive accuracy and mitigate overfitting. In RF, a random subset of features is selected for splitting the data, which trains multiple estimators on different aspects of the data, thereby reducing the likelihood of overfitting. Each decision tree is constructed using a randomly selected subset of data points and features, with individual trees being built for each sample. After generating outputs from all trees, the final prediction is determined by majority voting (for classification) or averaging (for regression), depending on the specific application[39].

Figure 6(a) presents the workflow chart of a dual-label RF regressor. The frequency and displacement parameter d are selected as labels, forming a training dataset vector V. Figure 6(b) and (d) illustrate sketches of the initial data set from CST Microwave Studio™. Figure 6(c) and (e) illustrate the data set of THz transmittances

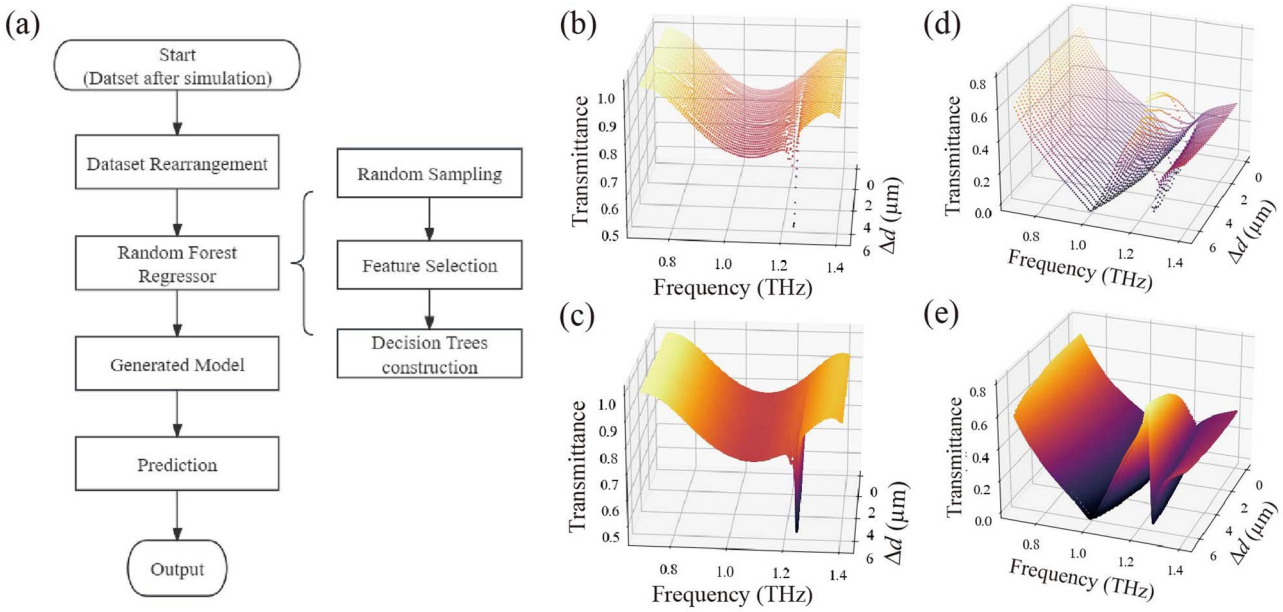


Fig. 6. Random Forest Regression for Pattern Recognition and prediction: (**a**) Schematic diagram of the RF process. (**b**) Simulated software transmittances data points under excitation perpendicular to the gap. (**c**) Overview of ML padded data to (**c**). (**d**) Simulated software transmittances data points under excitation parallel to the gap. (**e**) Overview of ML padded data to (**d**).

as function of frequency and displacement Δd calculated by RF regressor. The dual-label RF regressor help achieving a higher dataset density compared to manual simulation using CST Microwave Studio™, which acquired high prediction accuracy with a faster computational speed.

Data availability

Data underlying the results presented in this paper are not publicly available at this time but may be obtained from the authors upon reasonable request. C. J. should be contacted if someone wants to request the data from this study.

Received: 24 February 2025; Accepted: 29 July 2025
Published online: 31 July 2025

References

1. Li, D. et al. Metamaterial Terahertz sensor for measuring thermal-induced denaturation temperature of insulin. *IEEE Sens. J.* **20**, 1821–1828 (2020).
2. Park, S. J. et al. Detection of microorganisms using Terahertz metamaterials. *Sci. Rep.* **4**, 4988 (2014).
3. Wu, X. et al. Alkanethiol-functionalized Terahertz metamaterial as label-free, highly-sensitive and specific biosensor. *Biosens. Bioelectron.* **42**, 626–631 (2013).
4. Xie, L., Gao, W., Shu, J., Ying, Y. & Kono, J. Extraordinary sensitivity enhancement by metasurfaces in Terahertz detection of antibiotics. *Sci. Rep.* **5**, 8671 (2015).
5. Zhang, W. et al. Terahertz metamaterials for biosensing applications: a review. *Biosensors* **14**, 3 (2024).
6. Xu, H. et al. Identifying phenotypes of colorectal malignant tumors using the quasi-bound state in the continuum of a Terahertz metasurface biosensor. *Biomed. Opt. Express.* **16**, 1471 (2025).
7. Xue, Y. et al. The impact of contact and contactless interactions between the meta-atoms on Terahertz bound States in the continuum. *J. Phys. Appl. Phys.* **57**, 55103 (2024).
8. Wang, X. et al. Exploiting universal nonlocal dispersion in optically active materials for spectro-polarimetric computational imaging. *Elight* **4**, 22 (2024).
9. Wang, Z. Y. et al. Vectorial liquid-crystal holography. *Elight* **4**, 5 (2024).
10. Hsu, C. W., Zhen, B., Stone, A. D., Joannopoulos, J. D. & Soljačić, M. Bound States in the continuum. *Nat. Rev. Mater.* **1**, 16048 (2016).
11. Marinica, D. C., Borisov, A. G. & Shabanov, S. V. Bound States in the continuum in photonics. *Phys. Rev. Lett.* **100**, 183902 (2008).
12. Liu, P. et al. Governance of friedrich–wintgen bound States in the continuum by tuning the internal coupling of meta-atoms. *Opt. Lett.* **49**, 1301 (2024).
13. Fan, J. et al. Hybrid bound States in the continuum in Terahertz metasurfaces. *Opto-Electron Sci.* **2**, 23006 (2023).
14. Fedotov, V. A., Rose, M., Prosvirnin, S. L. & Papasimakis, N. Zheludev, N. I. Sharp trapped-mode resonances in planar metamaterials with a broken structural symmetry. *Phys. Rev. Lett.* **99**, 147401 (2007).
15. Cai, Y., Huang, Y., Zhu, K. & Wu, H. Symmetric metasurface with dual band polarization-independent high-Q resonances governed by symmetry-protected BIC. *Opt. Lett.* **46**, 4049 (2021).
16. Cong, L. & Singh, R. Symmetry-protected dual bound States in the continuum in metamaterials. *Adv. Opt. Mater.* **7**, 1900383 (2019).
17. Li, H. et al. Photonic spin-selective perfect absorptance on planar metasurfaces driven by chiral quasi-bound States in the continuum. *Nanoscale* **15**, 6636–6644 (2023).

18. Dong, A. et al. Photonic-spin-controlled second-order nonlinear frequency conversion on permittivity-asymmetry lithium niobite dimer metasurfaces governed by chiral quasibound States in the continuum. *Phys. Rev. B*. **111**, 75301 (2025).
19. Zhou, Y. et al. Asymmetric tetramer metasurface sensor governed by quasi-bound States in the continuum. *Nanophotonics* **12**, 1295–1307 (2023).
20. Zhou, M. et al. Bound States in the continuum in all-dielectric metasurfaces with scaled lattice constants. *Sci. China Phys. Mech. Astron.* **66**, 124212 (2023).
21. Wang, S. Y. et al. Giant strong coupling in a Q-BICs' tetramer metasurface. *Opt. Lett.* **49**, 4154 (2024).
22. Zhao, Z. et al. Terahertz inner and outer edge modes in a tetramer of strongly coupled spoof localized surface plasmons. *Opt. Lett.* **48**, 1343 (2023).
23. Wang, Y., Han, Z., Du, Y. & Qin, J. Ultrasensitive Terahertz sensing with high- *Q* toroidal dipole resonance governed by bound States in the continuum in all-dielectric metasurface. *Nanophotonics* **10**, 1295–1307 (2021).
24. Wang, L. et al. Polarization insensitive symmetry protected quasi-bound States in the continuum at Terahertz band. *J. Appl. Phys.* **130**, 233102 (2021).
25. Chen, J., Qian, C., Zhang, J., Jia, Y. & Chen, H. Correlating metasurface spectra with a generation-elimination framework. *Nat. Commun.* **14**, 4872 (2023).
26. Ma, W., Cheng, F. & Liu, Y. Deep-learning-enabled on-demand design of chiral metamaterials. *ACS Nano*. **12**, 6326–6334 (2018).
27. Zhu, R. et al. Phase-to-pattern inverse design paradigm for fast realization of functional metasurfaces via transfer learning. *Nat. Commun.* **12**, 2974 (2021).
28. Kiani, M., Kiani, J. & Zolfaghari, M. Conditional generative adversarial networks for inverse design of multifunctional metasurfaces. *Adv. Photonics Res.* **3**, 2200110 (2022).
29. Negm, A., Bakr, M. H., Howlader, M. M. R. & Ali, S. M. Deep learning-based metasurface design for smart cooling of spacecraft. *Nanomaterials* **13**, 3073 (2023).
30. Ding, Z. et al. Design of an ultra-broadband Terahertz absorber based on a patterned graphene metasurface with machine learning. *J. Mater. Chem. C*. **11**, 5625–5633 (2023).
31. Zhang, T. et al. Machine learning and evolutionary algorithm studies of graphene metamaterials for optimized plasmon-induced transparency. *Opt. Express*. **28**, 18899 (2020).
32. Jain, P. et al. Machine learning assisted hepta band THz metamaterial absorber for biomedical applications. *Sci. Rep.* **13**, 1792 (2023).
33. Kang, M., Zhang, S., Xiao, M. & Xu, H. Merging bound States in the continuum at off-high symmetry points. *Phys. Rev. Lett.* **126**, 117402 (2021).
34. *Machine Learning for Data Science Handbook: Data Mining and Knowledge Discovery Handbook* (Springer International Publishing, 2023). https://doi.org/10.1007/978-3-031-24628-9.
35. Khurgin, J., Bykov, A. Y. & Zayats, A. V. Hot-electron dynamics in plasmonic nanostructures: fundamentals, applications and overlooked aspects. *Elight* **4**, 15 (2024).
36. Garcia-Vidal, F. J. et al. Spoof surface plasmon photonics. *Rev. Mod. Phys.* **94**, 025004 (2022).
37. Liao, Z. et al. Guiding-mode-assisted double-BICs in an all-dielectric metasurface. *Opt. Express*. **30**, 24676–24688 (2022).
38. Zhou, C. et al. Optical radiation manipulation of Si-$Ge_2Sb_2Te_5$ hybrid metasurfaces. *Opt. Express*. **28**, 9690–9701 (2020).
39. Breiman, L. Random forests. *Mach. Learn.* **45**, 5–32 (2001).

Acknowledgements

This work is supported by the National Natural Science Foundation of China (NSFC) (Nos. 62475159) and The Fundamental Research Funds of Shaanxi Key Laboratory of Artificially-Structured Functional Materials and Devices (Nos. AFMD-KFJJ-24105). Jia and Zhao contributed equally in this work.

Author contributions

Z.Z. propose the original idea, C.J. conducted the simulation and wrote ML program, Z.Z. and C.J. analyzed the results. J. W. offers financial support. All authors reviewed the manuscript.

Declarations

Competing interests

The authors declare no competing interests.

Additional information

Correspondence and requests for materials should be addressed to Z.Z.

Reprints and permissions information is available at www.nature.com/reprints.

Publisher's note Springer Nature remains neutral with regard to jurisdictional claims in published maps and institutional affiliations.

Open Access This article is licensed under a Creative Commons Attribution-NonCommercial-NoDerivatives 4.0 International License, which permits any non-commercial use, sharing, distribution and reproduction in any medium or format, as long as you give appropriate credit to the original author(s) and the source, provide a link to the Creative Commons licence, and indicate if you modified the licensed material. You do not have permission under this licence to share adapted material derived from this article or parts of it. The images or other third party material in this article are included in the article's Creative Commons licence, unless indicated otherwise in a credit line to the material. If material is not included in the article's Creative Commons licence and your intended use is not permitted by statutory regulation or exceeds the permitted use, you will need to obtain permission directly from the copyright holder. To view a copy of this licence, visit http://creativecommons.org/licenses/by-nc-nd/4.0/.

© The Author(s) 2025